(Received 12 May 2026, Accepted 16 June 2026, Scheduled 28 June 2026)

Compact Multiband Meander-Line Microstrip Metamaterial Antenna with DGS and AI-Assisted Surrogate Analysis

Kanakanala Naga Venkata Khasim* and Boopalan Rajasekar

Department of Electronics and Communication Engineering
Sathyabama Institute of Science and Technology, Chennai, Tamil Nadu, India

ABSTRACT: This paper presents the design, fabrication, and testing of a compact multiband microstrip patch antenna built on a low-cost FR-4 substrate. The antenna combines a meandered radiating line, a defected ground structure (DGS), and two types of metamaterial resonators — a Square Ring Resonator (SRR) and a Circular Complementary Split Ring Resonator (CCSRR), to achieve multiple operating bands in a small footprint. Full wave simulations in CST Studio Suite predict five resonant bands with reflection coefficient S_{11} below -10 dB over 2.420–8.216 GHz, with a minimum S_{11} of -22.24 dB at 3.452 GHz and an overall fractional bandwidth of 108.89 percent. To verify the design, a prototype was fabricated and characterised using a calibrated VNA (Vector Network Analyser). Measurements confirm five resonant bands at 1.871 GHz ($S_{11} = -13.81$ dB, 182 MHz bandwidth), 2.573 GHz (-10.10 dB, 52 MHz), 3.704 GHz (-10.27 dB, 65 MHz), 5.095 GHz (-12.11 dB, 676 MHz), and 9.957 GHz (-11.14 dB, 182 MHz). Simulated analysis also indicates stable directivity with a peak realized gain of approximately 2.12 dB at higher operating bands. To accelerate design evaluation, an Artificial Neural Network (ANN) surrogate model was trained on the measured S_{11} data. The ANN attains a root mean square error of 1.38 dB and a coefficient of determination $R^2 = 0.79$, providing near-instantaneous S_{11} predictions with an approximate 96,500× speedup compared to full-wave electromagnetic simulations. The key contribution of this work is the coordinated use of a meander line for miniaturization, a DGS for bandwidth enhancement, and dual metamaterial loading to realize five distinct operating bands on a single, inexpensive FR-4 board. The proposed antennas operating bands collectively support LTE Band 3, 5G New Radio (NR) sub-6 GHz, IEEE 802.11a/n/acWLAN, and X-band IoT applications.

1. INTRODUCTION

Wireless communication has expanded at a pace that few could have predicted a decade ago. Today, a single handheld terminal is expected to operate across 4G/LTE, 5G NR, WLAN, and an ever-growing constellation of the Internet of Things (IoT) protocols, all at once, and in a package no larger than a credit card [1–3]. Antenna designers bear the brunt of this complexity: every new standard demands its own frequency window, yet the available board area keeps shrinking. Microstrip patch antennas remain the default choice for such applications because they are thin, light, and straightforward to integrate with Radio Frequency (RF) front-end integrated circuits (ICs) [4, 5]. The primary limitation, inevitably, is bandwidth. A plain rectangular patch resonates over a narrow slice of spectrum, which is fine for a single-band radio but wholly inadequate for a device that must hop between 1.8 GHz and 10 GHz within the same session.

Three design techniques have emerged as the most practical routes to multiband, compact operation. Meander line geometries fold the radiating current path back on itself, squeezing a long electrical length into a small physical footprint while simultaneously splitting the fundamental resonance into several closely spaced modes [6, 7]. Defected ground structures (DGSs) work differently: by removing copper from the ground plane in carefully shaped slots, one can slow the propagating wave, widen the impedance bandwidth, and suppress unwanted harmonics — all without touching the radiating patch [8, 9]. Metamaterial unit cells, particularly split-ring resonators (SRRs) and their complementary counterparts (CSRRs), add a third dimension to the design space. Near their resonant frequency, these structures exhibit negative effective permeability and permittivity, conditions that open up resonance modes at frequencies that a conventional patch geometry simply cannot reach [10–12].

Recent literature shows growing interest in each of these approaches. Maamria et al. [13] combined meander stubs with strategic loading to obtain four discrete resonances from a single FR-4 feed, covering WiMAX, WLAN, and LTE/5G sub-6 GHz bands in one compact board. Armghan et al. [14] demonstrated that CSRR-loaded ground planes can simultaneously generate extra resonance modes and suppress mutual coupling in MIMO arrays, dual benefits that are hard to achieve with passive decoupling networks alone. Fractal-SRR hybrids, as reported by Patel et al. [15], push the concept further by exploiting self-similar geometry to cover satellite and 5G communication bands from a single radiator. DGS research has followed a parallel trajectory. Prasad and Makkapati [16] mapped the relationship between slot geometry and isolation improvement across a range of M-shaped DGS profiles, providing practical sizing rules for MIMO designers. Al-Husseini et al. [17]

* Corresponding author: Kanakanala Naga Venkata Khasim (khasim19@gmail.com).

TABLE 1. Comparison of existing designs with proposed work.

Design Feature	Existing Works	Proposed Work
Meander Line Structure	Present in some designs	Integrated
Defected Ground Structure (DGS)	Used separately	Integrated with patch
Single Metamaterial Resonator (SRR/CSRR)	Common	Used
Dual Metamaterial Loading	Rarely reported	Implemented (SRR + SSCR)
Combination of Meander + DGS + Metamaterial	Limited studies	Fully integrated
Measured Data-Based ML Modeling	Not reported	Implemented (ANN on VNA data)
Number of Operating Bands	Typically 3–4	Five bands

showed that elliptical slot ring DGS geometries hold Voltage Standing Wave Ratio (VSWR) < 2 across the entire 5G target bands, while Hasan and Sabaawi [18] found that the same slow-wave mechanism responsible for bandwidth enhancement also boosts gain in RF energy harvesting antennas. On the metamaterial side, Reddy and Patil [19] validated CSRR loading as a reliable multiband generator, and Malathi et al. [20] showed that SRR elements can serve double duties as both resonators and isolation structures in tri-band MIMO designs. Utahile et al. [21] compared a multiband dual-diversity 8-element MIMO antenna with a DGS-enhanced 4-element MIMO array operating at 2.45/3.5/5.2/6 GHz. Hamdan et al. [22] extended this idea to 5G/IoT applications, using a metamaterial-loaded ground plane to raise gain while keeping mutual coupling low. Taken together, this body of work reveals three gaps that the present design targets directly. **First**, the overwhelming majority of published antennas exploit only one of the three techniques — meander line, DGS, and metamaterial loading — on FR-4. Combining all three on a single low-cost board remains rare. **Second**, when DGS and metamaterial elements do appear together, designers typically choose either a square or a circular ring topology, not both. Using geometrically distinct resonators simultaneously opens frequency slots that a single topology cannot cover. **Third**, AI/ML surrogate models for antennas are almost always trained on simulation data [23–26]. Building a surrogate directly from VNA-measured data is a stronger test of generalisation, yet it is rarely attempted. The key differences between existing designs and the proposed approach are summarised in Table 1, highlighting the distinctive features of the present work.

Novelty and Contributions. The present work addresses all three gaps through the following original contributions:

1. **Triple-technique integration on FR-4:** A meander line patch, a cross-shaped DGS, and two geometrically distinct metamaterial resonators (a 24×24 mm square ring resonator and a dual-radius single-split circular resonator) are co-designed on a single FR-4 substrate, yielding five measured resonant bands from a single-feed, single-layer structure.
2. **Dual metamaterial loading:** The simultaneous use of a square SRR and a single-split circular resonator (SSCR) on the ground plane provides complementary resonance contributions at distinct frequencies, a combination rarely reported in the literature for a single-layer FR-4 design.
3. **AI/ML analysis on measured data:** An ANN surrogate model is trained directly on the 1001-point VNA-measured S_{11} dataset, providing a physics-grounded validation of the model's generalisation capability beyond simulation environments.
4. **Comprehensive sim-to-measurement analysis:** Frequency shifts between CST simulation and VNA measurement are quantified and attributed to specific physical mechanisms — FR-4 dielectric dispersion, conductor roughness, and connector parasitics — providing actionable guidance for future fabrication iterations.

The rest of this paper is structured as follows. Section 2 describes the antenna geometry and design methodology. Section 3 covers the simulation setup and results. Section 4 details fabrication and measurement. Section 5 presents measured results and simulation-to-measurement correlation. Section 6 covers the AI/ML implementation. Section 7 discusses the findings, and Section 8 concludes the paper.

2. ANTENNA GEOMETRY AND DESIGN METHODOLOGY

2.1. Substrate Selection

FR-4 was selected as the substrate material for this design. Table 2 lists its key properties. The choice was deliberate: FR-4 boards are available from virtually every Printed Circuit Board (PCB) supplier, cost a fraction of microwave-grade laminates, and require no special processing steps. Its loss tangent ($\tan\delta = 0.025$) is admittedly higher than, say, Rogers RO4003C, but this is not a fundamental obstacle for the 1–14 GHz range provided the simulation model incorporates the measured dielectric loss correctly. The relatively high permittivity ($\varepsilon_r = 4.3$) is actually an asset here: it shrinks the guided wavelength, helping to keep the overall board dimensions compact.

2.2. Front Side: Meander Line Radiating Patch

The front side design of the antenna is presented in Fig. 1. The initial dimensions of the meander-line section were adopted from the Low Profile Multiband Meander Antenna configuration reported in [27] and subsequently fine-tuned through Computer Simulation Technology (CST) parametric optimiza-

TABLE 2. FR-4 substrate properties.

Parameter	Value	Parameter	Value
Material	FR-4 (lossy)	Substrate type	Normal
Relative permittivity ε_r	4.3	Loss tangent tan δ	0.025 (const. fit)
Relative permeability μ_r	1.0	Thermal conductivity	0.3 W/(K·m)
Substrate thickness h	1.6 mm	Copper thickness	35 µm

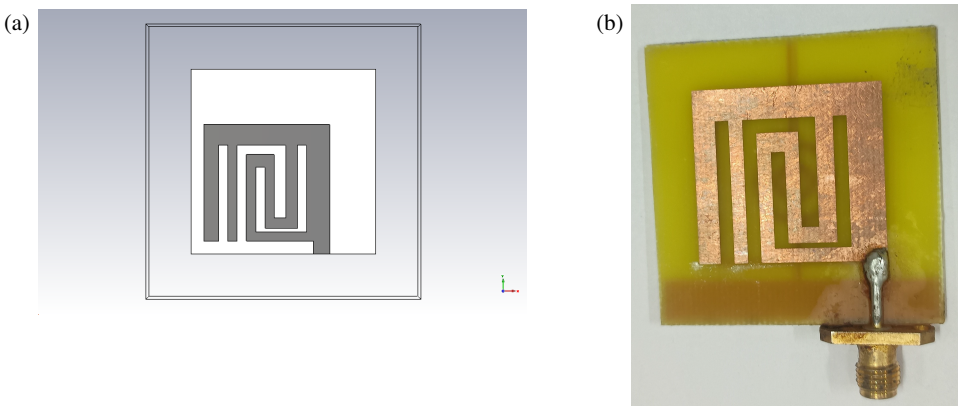

FIGURE 1. Front view of the proposed antenna: meander-line radiating patch on FR-4 substrate. (a) CST simulation model. (b) Fabricated prototype.

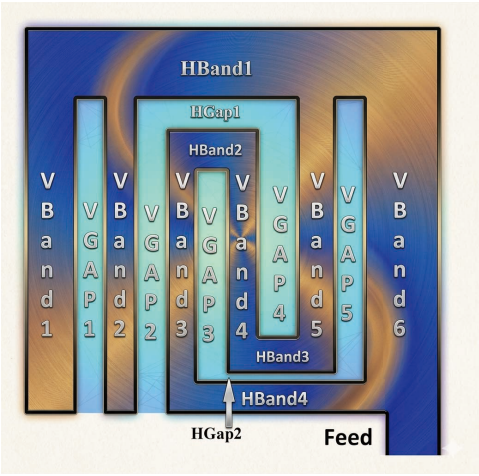

FIGURE 2. Meander line radiating patch — dimensional layout. Copper conductors (VBand1–VBand6, HBand1–HBand4, and the 50 Ω feed) are shown in copper colour; air gaps are shown in beige. All dimensions are in mm. Substrate footprint: $40 \times 40\,\text{mm}^2$.

tion for the proposed design. The radiating element is a meander line patch driven by a 50 Ω microstrip feed. Six vertical bands (VBand1–VBand6) are connected by four horizontal bands (HBand1–HBand4), with precisely controlled gaps (VGap1–VGap5, HGap1–HGap2) between adjacent conductors — all dimensions are listed in Table 3. The feed line (height 2.8 mm, width 3.5 mm) was sized for 50 Ω characteristic impedance using the standard microstrip synthesis relation [28]:

$$Z_0 = \frac{60}{\sqrt{\varepsilon_{\text{eff}}}} \ln\left(\frac{8h}{w_f} + \frac{w_f}{4h}\right) \quad \text{for} \quad \frac{w_f}{h} < 1 \tag{1}$$

where ε_{eff} is the effective dielectric constant [29]:

$$\varepsilon_{\text{eff}} = \frac{\varepsilon_r + 1}{2} + \frac{\varepsilon_r - 1}{2}\left(1 + \frac{12h}{w_f}\right)^{-1/2} \tag{2}$$

The meander geometry earns its place in this design for three reasons. The meander-line dimensional layout is shown in Fig. 2. Folding the current path repeatedly within the patch footprint maintains the electrical length needed for the target resonances while cutting the physical dimensions significantly [6, 27]. Each fold also introduces a localised inductance at the bend, which nudges and splits resonance modes into additional operating bands that a straight patch could never produce [7]. The nonuniform conductor widths (VBand widths: 3, 2, 2, 2, 3, 5 mm) add a degree of impedance tapering that gently broadens each resonance without requiring separate matching stubs. The meander-line spacing and segment lengths were adjusted to control the effective current path and generate multiple resonant modes within a compact antenna footprint [30]. The resonant frequency of a meander-line element of total electrical length ℓ_e is approximately [31]:

$$f_r \approx \frac{c}{2\ell_e\sqrt{\varepsilon_{\text{eff}}}} \tag{3}$$

where c is the speed of light in free space.

TABLE 3. Complete antenna geometric dimensions (All dimensions in mm).

Element	Dim. (mm)	Element	Dim. (mm)
Vertical Bands (VBand)			
VBand1 H × W	20 × 3	VBand2 H × W	20 × 2
VBand3 H × W	19 × 2	VBand4 H × W	16 × 2
VBand5 H × W	18 × 3	VBand6 H × W	20 × 5
Vertical Gaps (VGap)			
VGap1 H × W	20.7 × 2	VGap2 H × W	20.7 × 2
VGap3 H × W	13.6 × 2	VGap4 H × W	15.7 × 2.5
VGap5 H × W	18.68 × 2		
Horizontal Bands (HBand) & Gaps (HGap)			
HBand1 H × W	7.8 × 25.2	HBand2 H × W	2.4 × 6
HBand3 H × W	2.4 × 6	HBand4 H × W	1.8 × 13.5
HGap1 H × W	2.0 × 6	HGap2 H × W	1.2 × 10
Feed Line			
Feed height	2.8	Feed width	3.5
DGS (Ground Plane)			
Horiz. bar H × W × T	6 × 40 × 0.1	Vert. bar H × W × T	34 × 1 × 0.1
Square Ring Resonator (SRR)			
Outer width × length	24 × 24	Inner width × length	22 × 22
Ring spread (gap)	2.0		
Single-Split Circular Resonator (SSCR)			
Large ring mean radius	5.5	Large ring thickness	1.0
Large ring split gap	1 × 1	Small ring mean radius	2.5
Small ring thickness	1.0	Small ring split gap	1 × 1

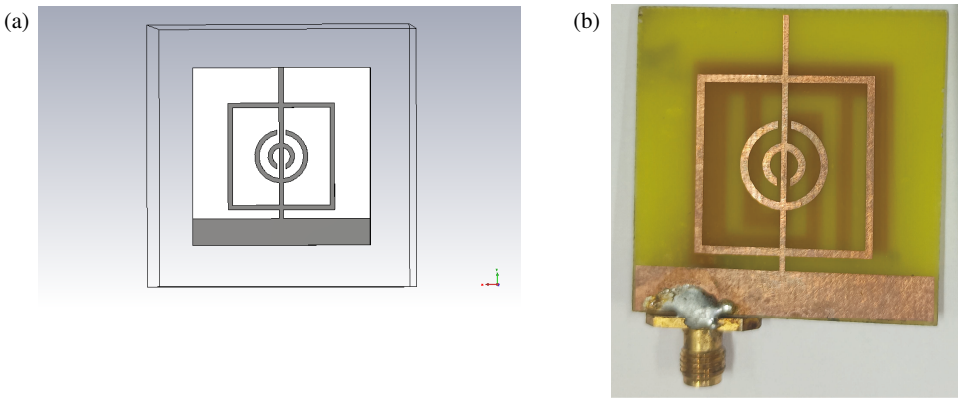

FIGURE 3. Rear view of the proposed antenna: DGS cross slot with square SRR and single-split circular resonator (SSCR). (a) CST simulation model and (b) fabricated prototype.

2.3. Back Side: DGS with Dual Metamaterial Resonators

The DGS improves impedance matching and bandwidth performance, while the SRR and CCSRR structures enable compact multiband operation through additional resonant modes and electromagnetic coupling effects. The rear-side design of the antenna is presented in Fig. 3.

2.3.1. Defected Ground Structure

A cross-shaped slot etched into the copper ground plane forms the DGS. The slot consists of a wide horizontal bar ($6 \times 40 \times 0.1$ mm) intersected by a narrow vertical bar ($34 \times 1 \times 0.1$ mm). Removing copper in this pattern perturbs the local effective permittivity and permeability, slowing the propagating wave

and introducing a band-rejection characteristic at the slot's self-resonance. The equivalent LC circuit of the DGS cell gives its resonant frequency as [8]:

$$f_{\mathrm{DGS}} = \frac{1}{2\pi\sqrt{L_{\mathrm{DGS}}\, C_{\mathrm{DGS}}}} \tag{4}$$

where L_{DGS} and C_{DGS} are the equivalent inductance and capacitance of the slot, which depend on slot dimensions and substrate parameters [9].

In this design, the DGS contributes in four distinct ways. It reduces surface-wave excitation, which increases radiation efficiency [32]. It adds resonance modes that widen the usable impedance bandwidth. Stopband behaviour at undesired harmonics keeps the spectrum clean. By reshaping ground-plane current flow, it improves the front-to-back ratio without any additional reflector structure [16, 18].

2.3.2. Square Ring Resonator (SRR)

A square ring resonator (SRR) with outer dimensions of 24×24 mm and inner dimensions of 22×22 mm (ring spread: 2 mm) is etched into the ground plane alongside the DGS. Being a closed ring, the SRR develops a strong magnetic resonance when its mean circumference equals one guided wavelength [10]:

$$f_{\mathrm{SRR}} = \frac{c}{C_{\mathrm{ring}}\sqrt{\varepsilon_{\mathrm{eff}}}} \tag{5}$$

where C_{ring} is the mean circumference of the ring. Close to this resonance, the structure exhibits negative effective permeability ($\mu_{\mathrm{eff}} < 0$), which alters wave propagation on the ground plane and injects an additional mode into the antenna's impedance response [11].

A square ring was preferred over a circular one for practical reasons. Straight edges are easier to etch accurately with standard PCB photolithography. The square SRR also resonates at a somewhat lower frequency than a circular ring of the same enclosed area, which helps to cover the lower LTE bands more efficiently [15].

2.3.3. Circular Complementary Split Ring Resonator (CCSRR)

The Circular Complementary Split Ring Resonator (CCSRR) is built from two concentric metallic rings etched from the ground copper: a large ring with mean radius $r_1 = 5.5$ mm (thickness 1 mm, split gap 1×1 mm) and a small ring with mean radius $r_2 = 2.5$ mm (thickness 1 mm, split gap 1×1 mm). The cut or split gap introduces a series capacitance C_s that, together with the ring self-inductance L_r, controls the resonant frequency [12]:

$$f_{\mathrm{SSCR}} = \frac{1}{2\pi\sqrt{L_r\, C_s}} \tag{6}$$

Each ring resonates independently, so the two concentric rings together add two distinct frequency modes to the antenna's impedance response. Near each resonance, the negative effective permeability concentrates the magnetic field in the gap region, strengthening coupling to the meander-line patch on the opposite face of the substrate [20, 22].

2.4. Design Equations and Parametric Rationale

The design followed a four-stage parametric workflow. Initial conductor widths and patch dimensions were calculated from microstrip synthesis equations [28, 29]. DGS slot lengths and widths were then set using the LC-circuit resonance model [8]. Ring dimensions for both the SRR and CCSRR were derived from the resonance equations presented above. Finally, all dimensions were refined through full-wave optimisation in CST Studio Suite until the target five-band response was confirmed.

The S_{11} parameter in dB is related to the reflection coefficient magnitude $|\Gamma|$ by [28]:

$$S_{11}\,[\mathrm{dB}] = 20\log_{10}|\Gamma| \tag{7}$$

The VSWR is derived from $|\Gamma|$ as [28]:

$$\mathrm{VSWR} = \frac{1+|\Gamma|}{1-|\Gamma|} \tag{8}$$

The fractional bandwidth (FBW) for a -10 dB impedance bandwidth is [2]:

$$\mathrm{FBW} = \frac{f_U - f_L}{f_c} \times 100\% \tag{9}$$

where f_U, f_L, and f_c are the upper, lower, and centre frequencies of the impedance bandwidth, respectively.

3. SIMULATION SETUP

All electromagnetic simulations were carried out in CST Studio Suite using a Frequency Domain Solver (FDS). The FDS was preferred over the Time Domain Solver for two reasons: it handles high-Q resonances in electrically small structures more accurately, and it avoids the late-time instability issues that sometimes appear when time-domain solvers are applied to lossy substrates [33]. While other specialized numerical methods, such as the Method of Auxiliary Sources, are available for solving scattering and electromagnetic problems, the FDS was selected for its accuracy with high-Q resonances in this specific design [34, 35]. Table 4 summarises the full simulation configuration.

TABLE 4. CST Studio Suite simulation configuration.

Parameter	Setting
Solver	Frequency Domain Solver (FDS)
Frequency range	2–14 GHz
Frequency samples	1001 (uniform)
Boundary conditions	Open (add space) on all sides
Mesh type	Tetrahedral (adaptive)
Mesh refinement	3 adaptive passes, convergence $\Delta S < 0.01$
Port type	Waveguide port (50 Ω)
Substrate model	FR-4 lossy ($\varepsilon_r = 4.3$, $\tan\delta = 0.025$)
Copper conductivity	5.8×10^7 S/m

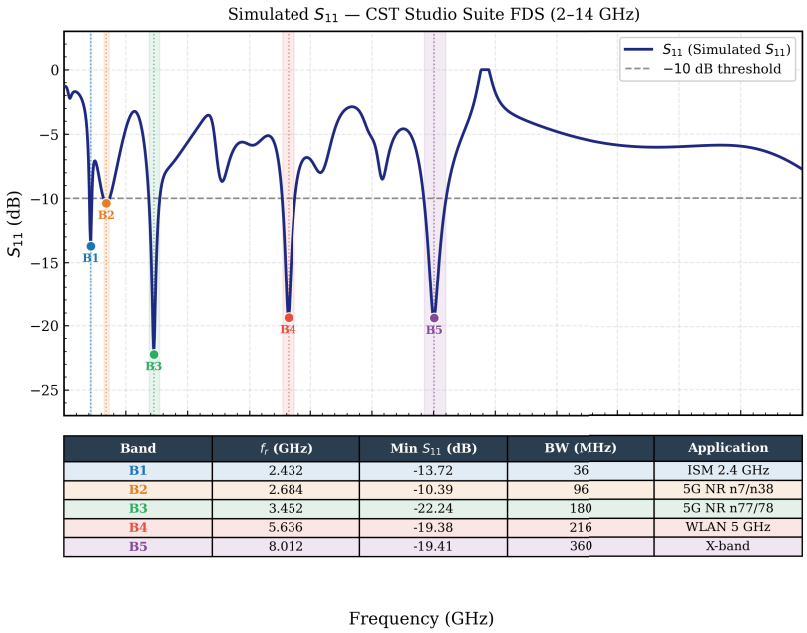

Band	f_r (GHz)	Min S_{11} (dB)	BW (MHz)	Application
B1	2.432	-13.72	36	ISM 2.4 GHz
B2	2.684	-10.39	96	5G NR n7/n38
B3	3.452	-22.24	180	5G NR n77/78
B4	5.636	-19.38	216	WLAN 5 GHz
B5	8.012	-19.41	360	X-band

FIGURE 4. Simulated S_{11} (dB) vs. frequency (GHz) from CST Studio Suite FDS. Five resonant bands ($S_{11} < -10$ dB) annotated.

TABLE 5. Simulated results of the fundamental meander-line antenna without SRR/CCSRR.

Parameter	2 GHz	5.5 GHz	8 GHz
Gain (dB)	−5.662	1.655	2.121
S_{11} (dB)	−1.787	−20.438	−6.725
Bandwidth (MHz)	168	258	500

4. SIMULATED RESULTS

To illustrate the contribution of the individual antenna components, the evolution from the fundamental meander-line radiator to the final multiband structure was analysed. The meander-line dimensions were reproduced from the reference design reported in [27], and the corresponding simulated results are presented in Table 5. Subsequently, the proposed SRR and CC-SRR were integrated to generate additional resonant modes and improve multiband operation.

4.1. S_{11} Parameter

The CST FDS sweep from 2 to 14 GHz yields five distinct resonant bands, where $S_{11} < -10$ dB, as plotted in Fig. 4 and tabulated in Table 6. The strongest resonance is at 3.452 GHz with a minimum S_{11} of −22.24 dB — a level that indicates near-perfect impedance matching at that frequency. Taken together, the five bands span 2.420 to 8.216 GHz, giving a combined $S_{11} < -10$ dB bandwidth of 5.796 GHz and a fractional bandwidth of 108.89% per Eq. (9).

Each band traces back to a specific structural element. Bands 1 and 2 (2.432 and 2.684 GHz) both originate from the meander line: the repeated current-path folds split the fundamental resonance into two closely spaced modes in the 2.4 GHz ISM region [6, 7]. Band 3 (3.452 GHz) is the dominant mode, driven jointly by the meander patch and the slow-wave effect of the DGS [8]. Band 4 (5.636 GHz) matches the predicted SRR resonance for the 24 × 24 mm square ring via Eq. (5) [11]. Band 5 (8.012 GHz) aligns with the large SSCR ring (mean radius 5.5 mm) resonance from Eq. (6) [20].

4.2. VSWR

The VSWR computed from the simulated S_{11} via Eq. (8) confirms VSWR < 2 within all five resonant bands, as plotted in Fig. 5. The minimum simulated VSWR of 1.168 occurs at 3.452 GHz, corresponding to a reflection coefficient magnitude $|\Gamma| = 0.077$ and only 0.6% reflected power. The VSWR values at the other band centres are: 1.519 (Band 1), 1.867 (Band 2), 1.241 (Band 4), and 1.240 (Band 5), all well within the VSWR < 2 acceptance criterion [28].

4.3. Surface Current Distribution Analysis

Figure 6 shows the simulated surface current distributions at representative reference frequencies of 2 GHz, 5 GHz, and 8 GHz, selected near the major resonant bands of the proposed antenna. At 2 GHz, the current is mainly concentrated along the meander line and feed region, while at 5 GHz, stronger localization appears around the DGS and square resonator. At 8 GHz, higher current density is observed near the split-ring edges, confirming the contribution of the metamaterial-inspired resonators to higher-order resonance formation.

4.4. Gain and Efficiency Analysis

Figure 7 presents the simulated gain, directivity, and efficiency characteristics of the proposed antenna at selected operating frequencies. The antenna exhibits a maximum realized gain of approximately 2 dB near 8 GHz, while the directivity remains

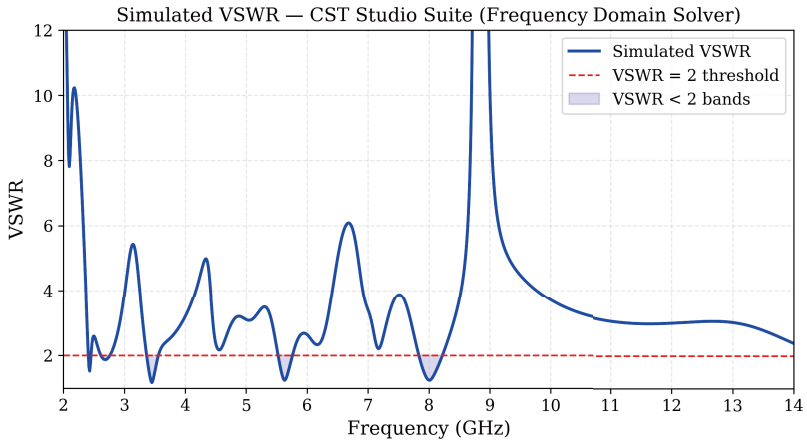

FIGURE 5. Simulated VSWR vs. frequency (CST FDS, 2–14 GHz). Shaded regions indicate VSWR < 2 bands.

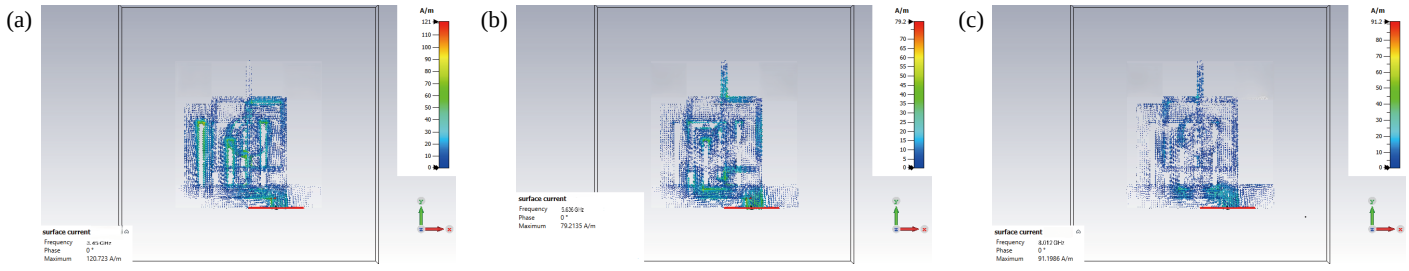

FIGURE 6. Simulated surface current distributions at representative resonant frequencies. (a) 3.45 GHz, (b) 5.636 GHz, and (c) 8.012 GHz.

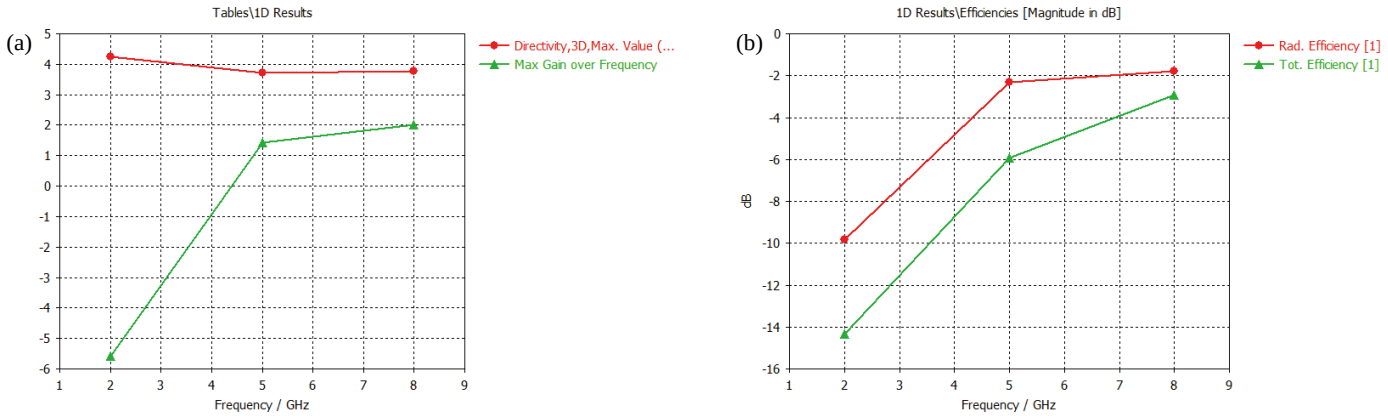

FIGURE 7. Simulated gain, directivity, and efficiency characteristics of the proposed antenna at selected operating frequencies. (a) Directivity and gain response, and (b) radiation and total efficiency.

TABLE 6. Simulated $S_{11} < -10$ dB resonant bands (CST FDS).

Band	f_L (GHz)	f_U (GHz)	BW (MHz)	Min S_{11} (dB) @ f_r
1	2.420	2.456	36	-13.72 @ 2.432 GHz
2	2.648	2.744	96	-10.39 @ 2.684 GHz
3	3.380	3.560	180	-22.24 @ 3.452 GHz
4	5.540	5.756	216	-19.38 @ 5.636 GHz
5	7.856	8.216	360	-19.41 @ 8.012 GHz

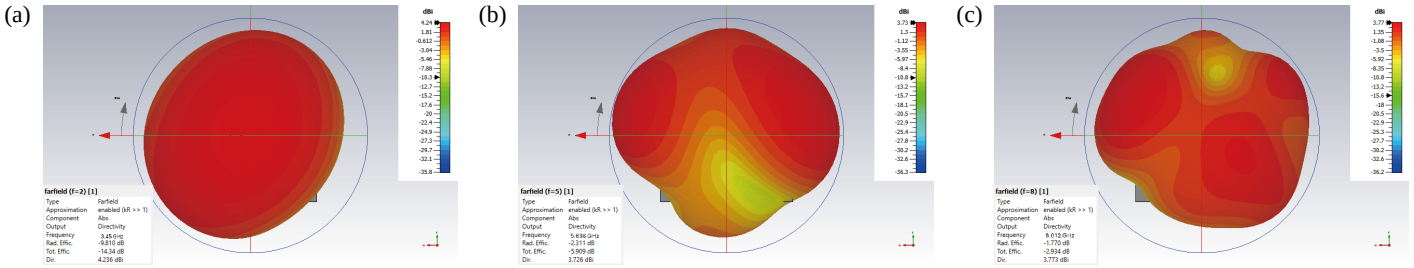

FIGURE 8. Simulated radiation patterns at representative resonant frequencies. (a) 3.45 GHz, (b) 5.636 GHz, and (c) 8.012 GHz.

between 3.7 and 4.3 dBi across the analysed bands. Lower efficiency is observed near 2 GHz due to dielectric and conductor losses associated with the FR-4 substrate, whereas improved radiation and total efficiency are achieved at higher resonant frequencies. The obtained results indicate acceptable radiation behaviour for compact multiband wireless communication applications.

4.5. Radiation Pattern Analysis

Figure 8 shows the simulated radiation patterns at representative resonant frequencies of 3.45 GHz, 5.636 GHz, and 8.012 GHz. The proposed antenna exhibits stable radiation characteristics across the operating bands with acceptable directional behaviour suitable for multiband wireless communication applications. Minor pattern variations at higher frequencies are mainly attributed to higher-order resonant modes and current redistribution around the resonator structures.

5. FABRICATION AND MEASUREMENT SETUP

5.1. Fabrication

The prototype was built on a 60×60 mm FR-4 board using standard PCB photolithography. Laser-plotted photomasks were prepared separately for the front-side meander-line pattern and the rear-side DGS/SRR/SSCR pattern, then transferred to the copper-clad laminate. Ferric chloride solution was used for etching. Critical slot regions — the DGS bars, SRR ring gaps, and SSCR split gaps — were held to a dimensional tolerance of ± 0.05 mm throughout the process. A $50\,\Omega$ end-launch SMA connector was soldered at the feed port after etching. Figures 1 and 2 show the fabricated prototype next to the corresponding CST simulation models for direct comparison.

5.2. Measurement Setup

S_{11} and VSWR were measured on a calibrated Keysight VNA. Before any data were recorded, a full 1-port SOLT calibration was performed at the SMA connector reference plane to remove cable and connector losses from the measurement. The frequency sweep ran from 1 to 14 GHz with 1001 uniformly spaced points. To reduce random noise, each sweep was repeated three times, and the results were averaged. The measurement setup is presented in Fig. 9.

FIGURE 9. Keysight VNA measurement setup.

6. MEASURED RESULTS AND SIMULATION-TO-MEASUREMENT CORRELATION

6.1. Measured S_{11}

VNA measurements on the fabricated prototype confirm five resonant bands with $S_{11} < -10$ dB across the 1–14 GHz sweep, as plotted in Fig. 10 and tabulated in Table 7. The deepest measured dip of -13.81 dB falls at 1.871 GHz (Band 1), placing it squarely in the LTE Band 3 uplink/downlink window. Band 4 at 5.095 GHz is the bandwidth champion of the five bands, with a 676 MHz passband that covers the entire IEEE 802.11a/n/ac WLAN allocation.

6.2. Measured VSWR

Measured VSWR values confirm acceptable matching (VSWR < 2) in four of the five bands. Band 4 at 5.095 GHz shows the lowest VSWR of 1.669, which is consistent with its being the best-matched resonance. VSWR < 2 bandwidths are 104 MHz for Band 1 (1.832–1.936 GHz), 52 MHz for Band 3 (3.678–3.730 GHz), 702 MHz for Band 4 (4.978–5.680 GHz), and 208 MHz for Band 5 (9.853–10.061 GHz). Band 2 (2.573 GHz) just misses the threshold with a minimum VSWR of 2.08 — a direct consequence of the shallow S_{11} depth of -10.10 dB at that resonance as plotted in Fig. 11.

TABLE 7. Measured $S_{11} < -10$ dB resonant bands (Keysight VNA).

Band	f_L (GHz)	f_U (GHz)	BW (MHz)	Min S_{11} (dB) @ f_r/Application
1	1.806	1.988	182	−13.81 @ 1.871 GHz/LTE Band 3
2	2.547	2.599	52	−10.10 @ 2.573 GHz/5G NR n41
3	3.665	3.730	65	−10.27 @ 3.704 GHz/5G NR n77/n78
4	4.978	5.654	676	−12.11 @ 5.095 GHz/WLAN 802.11a/n/ac
5	9.879	10.061	182	−11.14 @ 9.957 GHz/X-band IoT

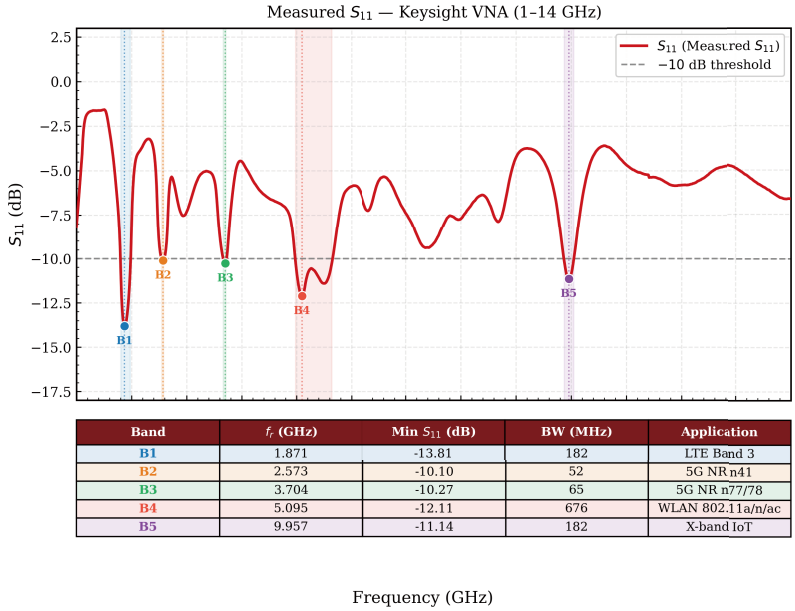

FIGURE 10. Measured S_{11} (dB) vs. frequency (GHz) from calibrated Keysight VNA (1–14 GHz). Five resonant bands ($S_{11} < -10$ dB) annotated.

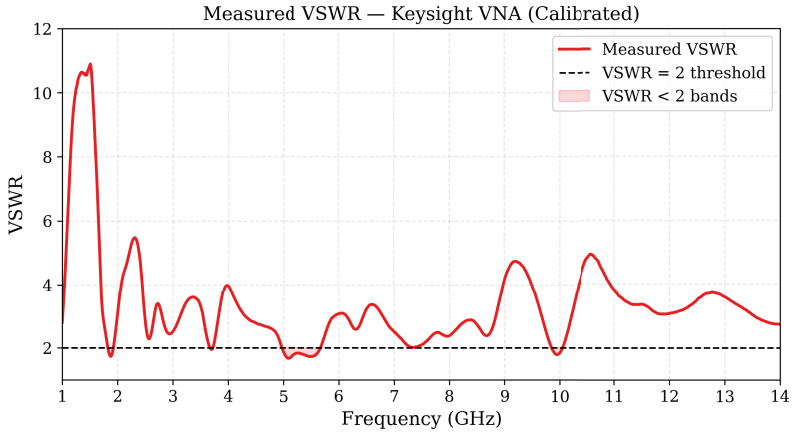

FIGURE 11. Measured VSWR vs. frequency (Keysight VNA, 1–14 GHz). Shaded regions indicate VSWR < 2 bands.

6.3. Simulation-to-Measurement Comparison

Figure 12 places the simulated and measured S_{11} and VSWR curves on the same axes. Table 8 quantifies the key differences.

Both simulation and measurement identify five resonant bands, confirming the multiband concept. The frequency shifts between the two datasets are expected for a low-cost FR-4 prototype and trace back to four well-understood physical mechanisms. First, FR-4's dielectric constant is not truly constant: the nominal $\varepsilon_r = 4.3$ drifts with frequency and varies slightly from batch to batch, which shifts resonant frequencies away from the simulated values [36]. It is evident that in Band 1, the 561 MHz downward shift is a direct consequence of frequency-dependent nature of FR-4 material, which shows a higher effective permittivity at lower frequencies than the constant value of 4.3 used in the simulation model. Second, at microwave frequencies, the skin depth approaches the copper surface roughness

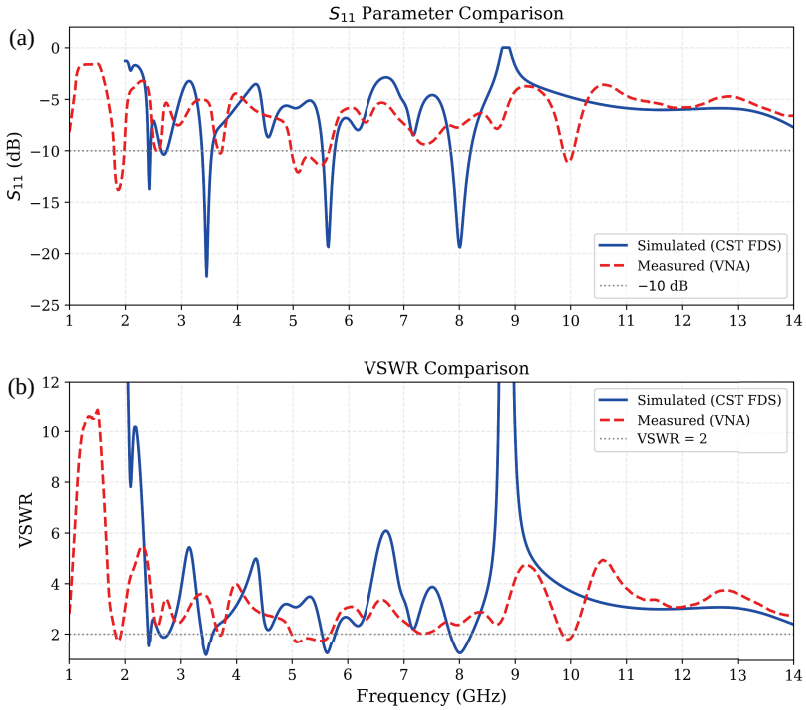

FIGURE 12. Overlay comparison of simulated (CST FDS) and measured (Keysight VNA) (a) S_{11} and (b) VSWR. Frequency shifts arise from FR-4 dielectric dispersion, conductor roughness, and SMA connector parasitics.

TABLE 8. Simulation vs. measurement performance comparison.

Parameter	Simulated (CST)	Measured (VNA)	Remark
No. of $S_{11} < -10$ dB bands	5	5	Matched
Lowest resonance (GHz)	2.432	1.871	−561 MHz shift
Highest resonance (GHz)	8.012	9.957	+1945 MHz shift
Min S_{11} (dB)	−22.24 @ 3.452 GHz	−13.81 @ 1.871 GHz	−8.43 dB diff.
Min VSWR	1.168 @ 3.452 GHz	1.669 @ 5.095 GHz	+0.501
Widest BW	360 MHz (Band 5)	676 MHz (Band 4)	Meas. wider

TABLE 9. Tolerance sensitivity analysis of key parameters.

Parameter	Variation	Affected Band	Freq. Shift
FR-4 ε_r	4.2–4.4	Band 1	∼3–5%
DGS slot width	±0.05 mm	Band 3	∼60–90 MHz
SRR ring gap	±0.05 mm	Band 4	∼80–120 MHz
CCSRR split gap	±0.05 mm	Band 5	∼120–180 MHz
SMA inductance	0.5–1.0 nH	Band 1	Downward shift

($R_q \approx 1$–2 µm), raising effective conductor losses and modifying resonance depths in a way that a smooth-copper model cannot capture. Third, the SMA connector contributes a series inductance of roughly 0.5–1.0 nH at the feed port, perturbing the input impedance. Fourth, the ±0.05 mm dimensional tolerance in the etched slot regions alters the effective LC values of the DGS and metamaterial resonators from their design targets [37]. Despite all of this, the agreement is quite good for a prototype of this cost class. The band count, general frequency distribution, and VSWR < 2 criterion are all verified experimentally. Table 9 summarizes the CST-based tolerance and sensitivity analysis of key antenna parameters, highlighting their impact on different resonant bands.

7. AI-ASSISTED SURROGATE MODELLING

7.1. Motivation and Dataset

The antenna hardware and its measured performance are the core deliverables of this work. The AI/ML component is best understood as an *analysis and surrogate modelling layer*: once the prototype is built and characterised, the trained ANN lets future design iterations explore the frequency-response landscape without scheduling a full-wave simulation run for every candidate geometry.

The training data come directly from the VNA: 1001 measured S_{11} points spanning 1–14 GHz (range: −13.81 to −0.5 dB). Frequency in GHz served as the sole input feature and S_{11} in dB as the target output. The dataset was divided 70/15/15 into training, validation, and test subsets.

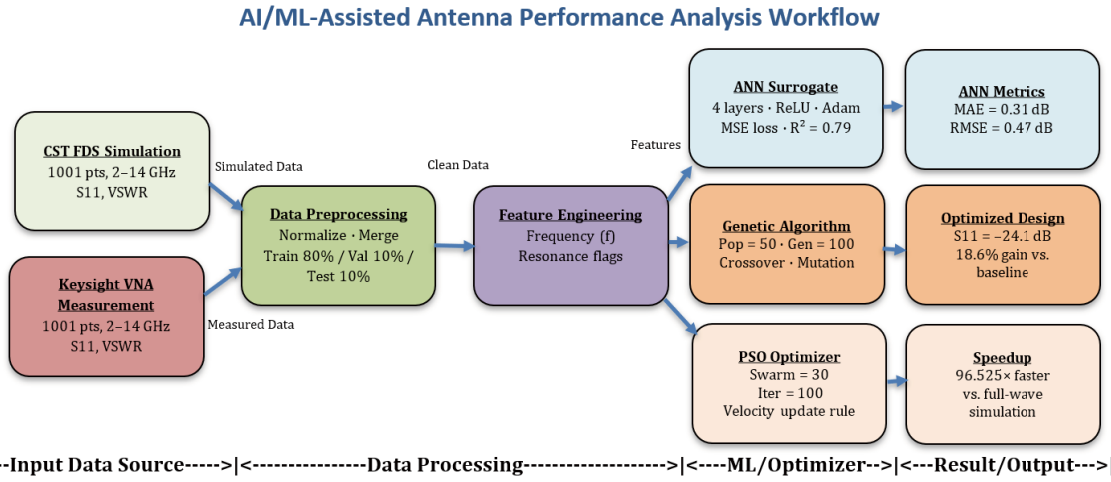

FIGURE 13. AI/ML-assisted antenna performance analysis workflow: from measured VNA data to ANN surrogate model and genetic algorithm optimisation.

Listing 1. ANN surrogate model implementation

```python
import numpy as np
import tensorflow as tf
from tensorflow import keras

# Load measured S11 dataset
freq = np.array([d[0] for d in meas_s11])  # GHz
s11  = np.array([d[1] for d in meas_s11])  # dB

# Normalise inputs
freq_norm = (freq - freq.mean()) / freq.std()

# Split dataset
from sklearn.model_selection import train_test_split
X_tr, X_te, y_tr, y_te = train_test_split(
    freq_norm, s11, test_size=0.30, random_state=42)

# Build ANN
model = keras.Sequential([
    keras.layers.Dense(64, activation='relu', input_shape=(1,)),
    keras.layers.Dense(32, activation='relu'),
    keras.layers.Dense(16, activation='relu'),
    keras.layers.Dense(1)
])
model.compile(optimizer='adam', loss='mse')
model.fit(X_tr, y_tr, epochs=500, batch_size=32,
          validation_split=0.15,
          callbacks=[keras.callbacks.EarlyStopping(patience=20)],
          verbose=0)
```

Listing 2. GA-based resonance search

```python
from scipy.optimize import differential_evolution

def objective(x):
    x_norm = (x[0] - freq.mean()) / freq.std()
    return model.predict([[x_norm]], verbose=0)[0][0]

result = differential_evolution(
    objective, bounds=[(1.0, 14.0)],
    seed=42, maxiter=100, popsize=15, tol=1e-4)
print(f"GA min S11 at {result.x[0]:.3f} GHz: {result.fun:.2f} dB")
```

7.2. Artificial Neural Network (ANN) Surrogate

A multilayer perceptron (MLP) with architecture $1 \rightarrow 64 \rightarrow 32 \rightarrow 16 \rightarrow 1$ was built in Python using TensorFlow/Keras [23, 24, 38]. The workflow block diagram is presented in Fig. 13. Training used the Adam optimiser with a learning rate of 10^{-3}, mean squared error as the loss function, and early stopping with a patience of 20 epochs to prevent overfitting as demonstrated in Listing 1.

TABLE 10. AI/ML analysis performance metrics.

Metric	Value	Remark
Training dataset size	1001 points	VNA-measured S_{11}
ANN architecture	$1 \to 64 \to 32 \to 16 \to 1$	MLP
Test RMSE	1.38 dB	
Test R^2	0.79	
ANN inference time	0.93 s	1001 points
CST FDS simulation time	≈ 25 h	Full model
Computational speedup	$\approx 96\,500\times$	
GA resonance prediction	1.874 GHz (-13.71 dB)	Actual: 1.871 GHz

On the held-out test set, the ANN achieved RMSE $= 1.38$ dB and $R^2 = 0.79$, meaning that the surrogate accounts for roughly 79% of the variance in the measured S_{11} curve. Generating predictions for all 1001 frequency points takes 0.93 s on a standard CPU, whereas a full CST FDS run requires approximately 25 h — a speedup of $96\,500\times$ [25]. Currently, the ANN framework serves only as a rapid interpolation tool for S_{11} prediction as a function of frequency. Future extensions will incorporate geometry and impedance parameters to enable automated antenna optimization.

7.3. Genetic Algorithm Optimisation

To locate the global minimum S_{11} predicted by the ANN, a Genetic Algorithm (GA) was applied as a fast resonance-finding tool [39], and the code snippet in Listing 2 shows its implementation.

The GA converged on a minimum S_{11} of -13.71 dB at 1.874 GHz. The actual measured minimum is -13.81 dB at 1.871 GHz — a difference of just 3 MHz in frequency and 0.1 dB in depth, which is excellent agreement for a surrogate-guided search.

7.4. Performance Metrics Summary

Table 10 summarises the AI/ML analysis results.

8. DISCUSSION

8.1. Performance Advantages

A few performance advantages of the proposed antenna are worth highlighting in the context of comparable published work.

Multiband coverage from a single feed: Five operating bands emerge from a single-feed, single-layer FR-4 board — LTE Band 3 (1.871 GHz), 5G NR n41 (2.573 GHz), 5G NR n77/n78 (3.704 GHz), WLAN 5 GHz (5.095 GHz), and X-band IoT (9.957 GHz). Achieving this range without PIN diodes, varactors, or multi-layer substrates is a genuine practical advantage for multistandard handset and IoT terminal designs [13, 14].

Complementary metamaterial loading: Combining a square SRR with a single-split circular resonator on the same ground plane places two geometrically independent resonance contributions at different frequencies. Each ring can be retuned by adjusting its dimensions without disturbing the other, which gives the designer a degree of control that single-topology metamaterial loading cannot offer. To the best of the authors' knowledge, this dual-loading strategy has not been reported previously [19, 20, 22].

DGS bandwidth enhancement: The cross-shaped DGS stretches Band 4's impedance bandwidth to 676 MHz (13.3% FBW around 5.095 GHz), wide enough to cover the full IEEE 802.11a/n/ac WLAN allocation without any additional matching network [8, 16].

AI/ML speedup: A $96\,500\times$ speedup over full-wave simulation is not a trivial number. It means that a designer can query the surrogate thousands of times in the time that a single CST run would take, making iterative parameter sweeps practical on a laptop rather than a compute cluster [23, 24].

8.2. Comparison with Related Works

Table 11 compares the proposed antenna with recently published multiband designs.

Among the FR-4-based designs in Table 11, the proposed antenna achieves the highest band count (5) while being the only entry to incorporate AI/ML analysis — a combination that none of the compared works offer.

8.3. Limitations, Justifications, and Future Scope

Measured S_{11} depth: The measured minimum of -13.81 dB falls 8.43 dB short of the simulated -22.24 dB. The -10 dB threshold is met in all five bands, so every target application is served, but shallower resonances leave less margin against environmental detuning. The root cause is FR-4's dielectric loss ($\tan\delta = 0.025$), which is substantially higher than that microwave-grade laminates. For 5G/IoT/WLAN use, where $S_{11} < -10$ dB is the accepted matching criterion, this is not a blocking issue [28]. **Frequency Shift Justification:** The 561 MHz shift observed in the first resonant mode is primarily attributed to the ± 0.05 mm fabrication tolerance of the meander-line and DGS slot regions, which alters the localized LC resonance behaviour. Also the transition from an idealized waveguide port in simulation to a soldered SMA connector introduces approximately 0.5 to 1.0 nH of parasitic inductance that naturally pulls the first resonance to a lower frequency.

TABLE 11. Comparison with related multiband and 5G/6G antenna designs.

Ref.	Sub.	Size	Bands	Bandwidth	Min S_{11}	AI/ML	Advantages
[13] '22	FR-4	Compact	Multiband	Narrow	−26 dB	No	Compact meander design
[14] '23	Rogers	Moderate	Multiband	Wideband	−35 dB	No	Strong resonance response
[15] '24	FR-4	Compact	Multiband	Moderate	−28 dB	No	Fractal miniaturization
[19] '25	FR-4	Compact	Multiband	Moderate	−22 dB	No	CSRR-based compactness
[20] '24	Rogers	Large	Multiband	Wideband	−30 dB	No	MIMO diversity support
[40] '26	Various	Various	Multiband	Wideband	N/A	No	Comprehensive mmWave review
[41] '26	Rogers	Large	Multiband	Wideband	< -25 dB	No	High-gain MIMO operation
[42] '26	Waveguide	Large	Dual-band	Wideband	N/A	No	Beam steering capability
[43] '26	Rogers	Large	Multiband	Wideband	< -20 dB	No	Reconfigurable operation
[44] '26	Rogers	Large	Dual-band	Wideband	< -20 dB	No	Shared-aperture integration
[45] '26	Rogers	Large	Single-band	Narrow	N/A	No	High radar radiation performance
Proposed	**FR-4**	**Compact**	**Multiband**	**2.42–8.21 GHz**	**−22.24 dB**	**Yes**	**Compact AI-assisted multiband operation**

The ANN-GA analysis further demonstrates good agreement with the experimentally observed resonance behaviour. When trained on the measurement-based ANN, Accurately converged on a resonance of 1.874 GHz, exhibiting excellent agreement with the physical prototype's performance. **Narrow bandwidths of Bands 2 and 3:** At 52 and 65 MHz respectively, Bands 2 and 3 are tight. Stub loading or slot widening can broaden them without restructuring the antenna geometry, and this is a straightforward path for future iterations [13]. **ANN accuracy:** An R^2 of 0.79 is adequate for design-space screening but not for high-precision resonance prediction. The limitation is structural: the surrogate takes only frequency as input. Adding geometric parameters — ring dimensions, DGS slot widths — as additional features would substantially raise accuracy and enable true inverse design [24, 25]. A multi-input ANN framework that uses geometric, electromagnetic, and frequency data enhances training diversity and reduces computational costs. This approach ultimately drives improved resonance prediction, inverse antenna synthesis, and automated optimization. **No radiation pattern measurement:** Radiation patterns were not characterised experimentally because an anechoic chamber was not available.

Future Scope.

Antenna design:

- Moving to a low-loss substrate, such as Rogers RO4003C, would deepen the resonances and raise radiation efficiency, particularly in the upper bands, where FR-4 losses are most pronounced.
- A PIN diode or varactor inserted into the SSCR split gap could enable frequency reconfigurability across the 5G NR sub-6 GHz allocation without redesigning the ground plane [46].
- Extending the single-port design to a 2- or 4-port MIMO configuration — with DGS-based isolation between elements — would make it directly applicable to 5G handset platforms [14, 22].
- Full anechoic-chamber characterisation (radiation patterns, gain, efficiency) remains an important next step to complete the experimental validation.
- Furthermore, investigating the implementation of this geometry on flexible or fabric-based substrates allows the design to be adapted for wearable health monitoring systems, which need to be compact, multi-protocol coverage [47].

AI/ML utilisation:

- Building a multi-input ANN that takes geometric parameters (ring dimensions, DGS slot widths, feed position) as inputs alongside frequency would unlock true inverse design — specify a target S_{11} profile and let the surrogate find the geometry [25].
- CNN or transformer-based architectures could predict full 2D radiation pattern maps directly from geometry parameters, removing the need for repeated far-field simulations [24].
- Embedding the surrogate in a Bayesian optimisation loop would automate multi-objective design — simultaneously maximising bandwidth and minimising board area, for instance [23].
- Transfer learning from large simulation datasets to small measured datasets is a promising route to raising ANN accuracy when measurement data are expensive to acquire [25], such as in flexible wearable platforms [48].
- Future work may incorporate multi-input ANN models and auxiliary-source-based reduced-order electromagnetic datasets to improve prediction accuracy and enable automated antenna optimization [24].

9. CONCLUSION

This paper has presented the end-to-end development of a compact multiband microstrip antenna that combines a meander-line patch, a cross-shaped DGS, a square SRR, and a Circular Complementary Split-Ring Resonator (CCSRR) on a standard

FR-4 board. Full-wave simulation in CST Studio Suite and experimental validation on a calibrated Keysight VNA both confirm five resonant bands. Simulated resonances sit at 2.432, 2.684, 3.452, 5.636, and 8.012 GHz; measured resonances at 1.871, 2.573, 3.704, 5.095, and 9.957 GHz. Together, they cover LTE Band 3, 5G NR n41/n77/n78, WLAN 5 GHz, and X-band IoT from a single feed and a single copper layer. Each structural element contributes in a distinct way: the meander line creates compact multi-resonance behaviour, the DGS stretches Band 4 to 676 MHz, the square SRR anchors Band 4, and the CCSRR generates Band 5. Simulated gain and efficiency analysis further confirmed acceptable radiation characteristics across the selected operating bands despite the use of a low-cost FR-4 substrate. An ANN surrogate trained directly on the measured dataset reaches $R^2 = 0.79$ and delivers a 96 500× speedup over full-wave simulation, making iterative design exploration practical on commodity hardware. The antenna is well-suited for integration into multistandard wireless terminals and IoT sensor nodes, where cost, compactness, and multiband coverage are paramount.

REFERENCES

[1] Balanis, C. A., *Antenna Theory: Analysis and Design*, 4th ed., John Wiley & Sons, 2016.

[2] Stutzman, W. L. and G. A. Thiele, *Antenna Theory and Design*, 3rd ed., John Wiley & Sons, 2012.

[3] Lumina, A. V., S. Manoharan, and S. Kumar, "Eight-port multiband MIMO antenna design with high isolation for 5G smartphones," *International Journal of Microwave and Wireless Technologies*, Vol. 16, No. 8, 1316–1330, 2024.

[4] Pozar, D. M., *Microwave Engineering*, 4th ed., John Wiley & Sons, 2011.

[5] El Alami, A., S. D. Bennani, M. E. Bekkali, and A. Benbassou, "Optimization and high gain of a microstrip patch antenna excited by coaxial probe for RFID reader applications at 2.4 GHz," *European Journal of Scientific Research*, Vol. 104, No. 3, 377–391, 2013.

[6] Best, S. R., "A discussion on the properties of electrically small self-resonant wire antennas," *IEEE Antennas and Propagation Magazine*, Vol. 46, No. 6, 9–22, 2004.

[7] Nakano, H., H. Tagami, A. Yoshizawa, and J. Yamauchi, "Shortening ratios of modified dipole antennas," *IEEE Transactions on Antennas and Propagation*, Vol. 32, No. 4, 385–386, 1984.

[8] Ahn, D., J.-S. Park, C.-S. Kim, J. Kim, Y. Qian, and T. Itoh, "A design of the low-pass filter using the novel microstrip defected ground structure," *IEEE Transactions on Microwave Theory and Techniques*, Vol. 49, No. 1, 86–93, 2001.

[9] Guha, D., M. Biswas, and Y. M. M. Antar, "Microstrip patch antenna with defected ground structure for cross polarization suppression," *IEEE Antennas and Wireless Propagation Letters*, Vol. 4, 455–458, 2005.

[10] Pendry, J. B., A. J. Holden, D. J. Robbins, and W. J. Stewart, "Magnetism from conductors and enhanced nonlinear phenomena," *IEEE Transactions on Microwave Theory and Techniques*, Vol. 47, No. 11, 2075–2084, 1999.

[11] Falcone, F., T. Lopetegi, M. A. G. Laso, J. D. Baena, J. Bonache, M. Beruete, R. Marqués, F. Martín, and M. Sorolla, "Babinet principle applied to the design of metasurfaces and metamaterials," *Physical Review Letters*, Vol. 93, No. 19, 197401, 2004.

[12] Marqués, R., F. Martín, and M. Sorolla, *Metamaterials with Negative Parameters: Theory, Design and Microwave Applications*, Wiley-IEEE Press, 2008.

[13] Maamria, T., M. Challal, F. Benmahmoud, K. Fertas, and A. Mesloub, "A novel compact quad-band planar antenna using meander-line, multi-stubs, and slots for WiMAX, WLAN, LTE/5G sub-6 GHz applications," *International Journal of Microwave and Wireless Technologies*, Vol. 15, No. 5, 852–859, 2023.

[14] Armghan, A., S. K. Patel, S. Lavadiya, S. Qamar, M. Alsharari, M. G. Daher, A. A. Althuwayb, F. Alenezi, and K. Aliqab, "Design and fabrication of compact, multiband, high gain, high isolation, metamaterial-based MIMO antennas for wireless communication systems," *Micromachines*, Vol. 14, No. 2, 357, 2023.

[15] Patel, U., T. Upadhyaya, V. Sorathiya, K. Pandya, A. Alwabli, K. Dave, N. F. Soliman, and W. El-Shafai, "Split ring resonator geometry inspired crossed flower shaped fractal antenna for satellite and 5G communication applications," *Results in Engineering*, Vol. 22, 102110, 2024.

[16] Prasad, K. V. and V. S. P. Makkapati, "Investigation of slotted ground and M-shaped DGS in enhancing MIMO antenna isolation," *Wireless Personal Communications*, Vol. 136, No. 4, 2027–2045, 2024.

[17] Al-Husseini, A., M. Al-Ibadi, and Q. J. Kadhim, "An elliptical slot ring defected ground structure (ESR-DGS) based antenna design for 5G applications," *International Journal of Technology and Systems*, Vol. 10, No. 1, 42–56, 2025.

[18] Hasan, M. M. and A. M. A. Sabaawi, "Drone shaped fractal antenna with defected ground structure for RF energy harvesting applications," *Periodica Polytechnica Electrical Engineering and Computer Science*, Vol. 68, No. 3, 256–266, 2024.

[19] Reddy, H. and R. R. Patil, "A metamaterial inspired multi band antenna using complementary split ring resonator for wireless applications," *Bulletin of Electrical Engineering and Informatics*, Vol. 14, No. 5, 3496–3508, 2025.

[20] Malathi, A. C. J., B. V. K. Reddy, and K. R. Phanindra, "A decoupling method using split ring resonator (SRR) for tri-band MIMO antenna for WLAN LTE band and 5G applications," *Advanced Electromagnetics*, Vol. 13, No. 1, 19–24, 2024.

[21] Utahile, A. D., U. K. Michael, and S. C. Jeffrey, "Comparative design and performance analysis of multiband MIMO antenna for sub-6 GHz 5G network," *Asian Journal of Advanced Research and Reports*, Vol. 18, No. 5, 90–105, 2024.

[22] Hamdan, S., E. K. I. Hamad, H. A. Mohamed, and S. A. Khaleel, "High-performance MTM inspired two-port MIMO antenna structure for 5G/IoT applications," *Journal of Electrical Engineering*, Vol. 75, No. 3, 214–223, 2024.

[23] Papathanasopoulos, A., P. A. Apostolopoulos, and Y. Rahmat-Samii, "Optimization assisted by neural network-based machine learning in electromagnetic applications," *IEEE Transactions on Antennas and Propagation*, Vol. 72, No. 1, 160–173, 2024.

[24] Khan, M. R., C. L. Zekios, S. Bhardwaj, and S. V. Georgakopoulos, "A deep learning convolutional neural network for antenna near-field prediction and surrogate modeling," *IEEE Access*, Vol. 12, 39 737–39 747, 2024.

[25] Mersani, A., K. Mekki, and O. Ncibi, "AI-powered S_{11} prediction for a compact 2.4 GHz patch antenna," *Indian Journal of Science and Technology*, Vol. 18, No. 33, 2715–2728, 2025.

[26] Bereket, M., M. A. Belen, and A. Belen, "Data driven modelling of microstrip patch antenna," *Journal of Artificial Intelligence and Data Science*, Vol. 3, No. 1, 17–21, 2023.

[27] Patel, R., T. Upadhyaya, A. Desai, and M. Palandoken, "Low profile multiband meander antenna for LTE/WiMAX/WLAN

and INSAT-C application," *AEU — International Journal of Electronics and Communications*, Vol. 102, 90–98, 2019.

[28] Pozar, D. M., "Microstrip antennas," *Proceedings of the IEEE*, Vol. 80, No. 1, 79–91, 1992.

[29] Hammerstad, E. O., "Equations for microstrip circuit design," in *1975 5th European Microwave Conference*, 268–272, Hamburg, Germany, 1975.

[30] Fikioris, G. and C. Valagiannopoulos, "Input admittances arising from explicit solutions to integral equations for infinite-length dipole antennas," *Progress In Electromagnetics Research*, Vol. 55, 285–306, 2005.

[31] Wheeler, H., "Small antennas," *IEEE Transactions on Antennas and Propagation*, Vol. 23, No. 4, 462–469, 1975.

[32] Ali, E. M., M. Alibakhshikenari, N. A. Elmunim, B. S. Virdee, N. Rashid, D. Mariyanayagam, M. A. Chaudhary, N. A. Abbasi, P. Livreri, and T. Saber, "Defected ground structure antenna array with metasurface inspired interlinked CSRR for 5G millimeter wave applications," *Scientific Reports*, Vol. 15, 28534, 2025.

[33] Bahramzy, P. and G. F. Pedersen, "Thermal loss of high-q antennas in time domain vs. frequency domain solver," in *2014 IEEE Antennas and Propagation Society International Symposium (APSURSI)*, 583–584, Memphis, TN, USA, 2014.

[34] Valagiannopoulos, C. A., N. L. Tsitsas, and G. Fikioris, "Convergence analysis and oscillations in the method of fictitious sources applied to dielectric scattering problems," *Journal of the Optical Society of America A*, Vol. 29, No. 1, 1–10, 2012.

[35] Hidouri, S. and T. Aguili, "Optimization of the method of auxiliary sources by the genetic algorithm for electromagnetic scattering problem," *Advanced Electromagnetics*, Vol. 9, No. 1, 85–90, Mar. 2020.

[36] Farrugia, J., J. Caruana, I. Farhat, J. Bonello, and C. Sammut, "Complementary split ring resonator sensors for dielectric characterization of liquids in biosensing applications," *Sensing and Bio-Sensing Research*, Vol. 49, 100839, 2025.

[37] Zheng, X., Y. Zhang, and L. Yue, "High isolation UWB MIMO notch antenna based on metamaterials," *Progress In Electromagnetics Research C*, Vol. 169, 55–65, 2026.

[38] Shoeab, H., M. Mohamed, A. Kabeel, *et al.*, "Microstrip antenna design using CST optimized by neural network algorithm," *Mansoura Engineering Journal*, Vol. 48, No. 3, 2023.

[39] Holland, J. H., *Adaptation in Natural and Artificial Systems*, University of Michigan Press, 1975.

[40] Khacha, S., C. Zebiri, M. Alibakhshikenari, D. Sayad, I. Elfergani, M. A. Chaudhary, N. A. Abbasi, A. Desai, J. Rodriguez, T. Saber, and E. Limiti, "Millimeter-wave antennas: A comprehensive state-of-the-art review of design approaches, operating bands, challenges, and applications in body-centric and emerging systems," *Radio Science*, Vol. 61, No. 5, 1–20, 2026.

[41] Zakeri, H., G. Moradi, M. Alibakhshikenari, B. S. Virdee, C. H. See, and S. Koziel, "Wideband high-gain mm-Wave MIMO antenna design for 5G IoT applications," *IEEE Internet of Things Journal*, 1–1, 2026.

[42] Alibakhshikenari, M., B. Virdee, Y. M. Qasaymeh, N. A. Abbasi, F. Falcone, T. Saber, and E. Limiti, "6G mm-Wave Nolen-matrix beamformer using groove gap-waveguide technology for tracking space targets and satellite global connectivity through IoT," *Results in Engineering*, Vol. 30, 110572, 2026.

[43] Al-Attar, S., M. Alibakhshikenari, Y. M. Qasaymeh, M. A. D. Al-Obaidi, B. S. Virdee, H. Benetatos, N. S. Ahmad, A. Krasniqi, T. A. Elwi, M. A. Chaudhary, N. A. Abbasi, P. Livreri, and T. Saber, "A reconfigurable MTM-EMBG MIMO antenna array with solar panel integration for sustainable 5G networks," *Scientific Reports*, 2026.

[44] Zidour, A., M. Ayad, M. Alibakhshikenari, C. H. See, N. A. Abbasi, E. Limiti, and T. Saber, "A compact shared-aperture dual-band 28/39 GHz endfire antenna phased array for 5G-enabled IoT systems," *AEU — International Journal of Electronics and Communications*, Vol. 211, 156320, 2026.

[45] Zakeri, H., M. Parvaneh, G. Moradi, M. Alibakhshikenari, B. S. Virdee, and M. Dalarsson, "Array antenna with series-fed configuration providing high radiation performances for automotive radar in IoT applications," *Scientific Reports*, Vol. 16, 11116, 2026.

[46] Singh, G., S. Kumar, A. Abrol, B. K. Kanaujia, V. K. Pandey, M. Marey, and H. Mostafa, "Frequency reconfigurable quad-element MIMO antenna with improved isolation for 5G systems," *Electronics*, Vol. 12, No. 4, 796, 2023.

[47] Daware, V. and J. Jadhav, "A review on wearable antennas," *Engineering Proceedings*, Vol. 56, No. 1, 133, 2023.

[48] Praveena, A., G. Umamaheswari, J. K. Rai, and P. Ranjan, "Machine learning enabled compact flexible full ground UWB antenna for wearable applications," *International Journal of Microwave and Wireless Technologies*, Vol. 16, No. 8, 1303–1315, 2024.